Article:
Ma, H., Sinclair, D.C. orcid.org/0000-0002-8031-7678 and Dean, J.S. orcid.org/0000-0001-7234-1822 (2023) A finite element study on the influence of surface cracks on micro-contact impedance spectroscopy measurements. Solid State Ionics, 393. 116173. ISSN: 0167-2738

https://doi.org/10.1016/j.ssi.2023.116173

Solid State Ionics 393 (2023) 116173

Contents lists available at ScienceDirect

Solid State Ionics

journal homepage: www.elsevier.com/locate/ssi

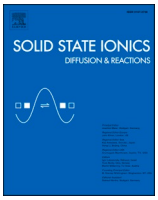

A finite element study on the influence of surface cracks on micro-contact impedance spectroscopy measurements

Hong Ma, Derek C. Sinclair, Julian S. Dean *

Department of Materials Science and Engineering, Sir Robert Hadfield Building, Mappin Street, Sheffield S1 3JD, UK

ARTICLE INFO

Keywords:
Finite element modeling
Micro-contact impedance spectroscopy
Impedance spectroscopy
Cracks and defects

ABSTRACT

Micro-contact impedance spectroscopy (MCIS) is a powerful tool to analyse local features of interest in electroceramics. The surface condition of the measured area of interest however may not always be ideal. Surface defects such as cracks may be present and therefore influence the measured MCIS data, especially for a top-top electrode configuration. Here we develop a finite element model on a system where a crack of various dimensions exists on the top surface between two surface micro-contact electrodes. We show how a crack can influence the current distribution within the sample and its effect in evaluating the MCIS data and associated extracted conductivity values. When the micro-contact separation is low, the hindrance effect forming from a crack acts to counterbalance the strong current interference effect that originates from closely placed top-top electrodes. The crack depth and length prove to be more effective than crack width in terms of counterbalancing interference. As the micro-contact separation increases, both current interference and crack hindrance decreases. Cracks in a specimen may therefore fortuitously assist in offsetting significant current interference effects, especially at the micro-contact separations used in many experimental set-ups.

1. Introduction

Impedance spectroscopy (IS) can be a powerful tool for analysing the electrical properties of various materials and devices [1]. In a conventional experimental setup, two macroscopic electrodes cover the outer surfaces of a sample/device and the impedance data generated measures the overall electrical response(s) within the entire sample [2] [3]. When local properties of a sample are of interest, micro-contact impedance spectroscopy (MCIS) is needed. The top-top micro-contact method uses an array of discrete micro-contacts (typically 10–30 μm in diameter) on the surface of a sample/device and has been used to probe specific regions such as surface layers, individual grains and grain boundaries in various ceramics and thick/thin films, eg [4–7]. Conventional IS uses a geometric factor to correct data for the influence of sample geometry, shown as Eq. 1, where σ is conductivity, t is the sample thickness, R is the measured resistance and A is the electrode area.

$$\sigma = \frac{t}{RA} \tag{1}$$

Top-top MCIS measurements take place in smaller regions of the sample surface which induces more complexity into data correction and analysis as the conventional geometric factor must be modified to be used in micro-contact experiments. A spreading resistance equation is widely used to extract sample conductivity.

For the configuration in Fig. 1 (a) where a micro-contact is placed on the top surface of a sample and the bottom surface is covered fully by a conventional counter electrode, the spreading resistance, R_{spr}, for a circular micro-contact of electrode radius, r:

$$R_{spr} = \frac{1}{4r_{mc}\sigma} \tag{2}$$

To apply this spreading resistance equation for this electrode arrangement, important requirements need to be met. These include that the spreading of the current density from the micro-contact can fully develop within the sample and there are no resistive regions that can block or hinder the current flow between the micro-contact and the counter electrode [8]. For the top-top configuration, where two micro-contacts are on the same surface and separated by a distance S, the spreading resistance equation is modified to become:

$$R_{spr} = \frac{1}{2r_{mc}\sigma} \tag{3}$$

for the scenario shown in Fig. 1 (b). The sample/electrode arrangements

* Corresponding author.
E-mail address: j.dean@sheffield.ac.uk (J.S. Dean).

https://doi.org/10.1016/j.ssi.2023.116173
Received 26 August 2022; Received in revised form 14 February 2023; Accepted 15 February 2023
Available online 24 February 2023

to obtain ideal spreading from micro-contacts are often not obtainable in MCIS, especially in the case of top-top arrangements, Fig. 1(b) and samples are seldom as electrically homogeneous as depicted in Figs. 1 (a) and (b). This is especially the case for electroceramic thin films grown on substrates and barrier coated samples where, cracks, pores, and interfaces (such as grain boundaries and between coating or film and substrate) are present, eg [9–11]. Other structural defects may be present and/or appear and develop with heat treatment, mechanical and/or electrical loading during experiments, eg [12]. There are various reports on the effects of such structural defects on MCIS measurements but in general, the MCIS response from a defective region is very different from a pristine or defect-free region. Lee et al. performed MCIS on nitrogen-graded 2 mol% yttria-doped tetragonal zirconia polycrystals (2Y-TZP) where micro-cracks appeared in samples annealed at 700 °C. Microcracks increased the scattering of the calculated conductivity values for annealed samples, whereas there was less deviation in values for as-prepared samples [13]. Wu et al. used MCIS to study failure detection in thermal barrier coatings. The sample contained an 8 wt% YSZ coating on a NiCrAlY bond coating with a nickel-based superalloy substrate. Cracks appeared in the YSZ layer after thermal cycling and their presence was attributed as the reason for the increase in measured impedance [14].

Understanding the effect of structural defects such as cracks on the impedance response based on MCIS would be valuable knowledge to add to the field. To achieve this, other factors such as variations in material composition within a sample, grain boundaries, grain shape and size etc., need to be eliminated from the experiment and/or model. Creating a single, electrically homogeneous material as a model with only a surface crack (of variable dimensions) can ensure that any change in the MCIS response from a top-top arrangement reflects the change in the crack settings within the model. This permits a systematic method to investigate the influence of surface cracks on MCIS measurements.

To achieve this goal, we have used finite element modeling (FEM) to create an idealised experimental set up. FEM is a powerful tool that can be used to simulate IS responses of various homogeneous and heterogeneous ceramics and can be used to reveal the relationship(s) between their electrical and physical microstructure(s), eg [15–17]. Veazey et al. used FEM to simulate the electrical responses from different MCIS electrode configurations on a cube of a homogenous single material with conductivity and permittivity of undoped $SrTiO_3$ at 300 °C [18]. This work demonstrated the importance of considering the influence of the electrode arrangements used in micro top-top MCIS measurements, in particular the S/r ratio and the physical location of the electrodes within the model. It highlighted there is a balance between two competing factors; (i) interference when contacts are placed close together and (ii) confinement where the electric field in unable to spread across the model/sample. To ensure neither of these effects influence the electrical measurements, they showed an S/r of 28 is required to limit interference, and the contacts placed at least 1.5r away from the edge of the sample to limit confinement. Under these conditions the measured (extracted) conductivity and permittivity from MCIS was the same as the input values from their model.

If the contacts are set closer together than shown in the 'ideal' schematic case in Fig. 1 (b), such as Fig. 1 (c) then interference in the current density arises from the overlapping spreading regions from each microcontact. This results in enhanced conductivity values being extracted from MCIS measurements. For example, S/r = 2 showed a conductivity enhancement of 23% compared to the input value. Clearly, a compromise is required as a typical microcontact radius of 5 μm would require S = 140 μm to obtain the correct conductivity. An S/r of 10 for r = 5 μm requires S = 50 μm and the measured conductivity is ~ + 10% of the input value which is much more experimentally feasible and gives acceptable accuracy from such measurements. Where possible, it is advisable to use S/r ~ 10 in experimental set-ups when using eq. (3) to extract conductivity values from MCIS.

The converse effect to interference is confinement where there is insufficient space for the current density to fully spread out from the microcontacts within the sample and therefore results in a reduction in the measured conductivity compared to the input value. This scenario can occur if electrodes are placed too close to the edges of the sample. This is typically a distance <1.5r, as shown schematically in Fig. 1 (d). Finally, for samples of very small dimensions with low S/r both interference and confinement effects can occur, see Fig. 1 (e). In some scenarios, the use of the spreading resistance equation remains valid as the competing factors balance sufficiently that extracted conductivity values can be within 10% of the input value. In other cases (especially for very thin samples), it is better to apply the geometric factor correction, eq. (1) as opposed to using a spreading resistance expression such as eq. (3).

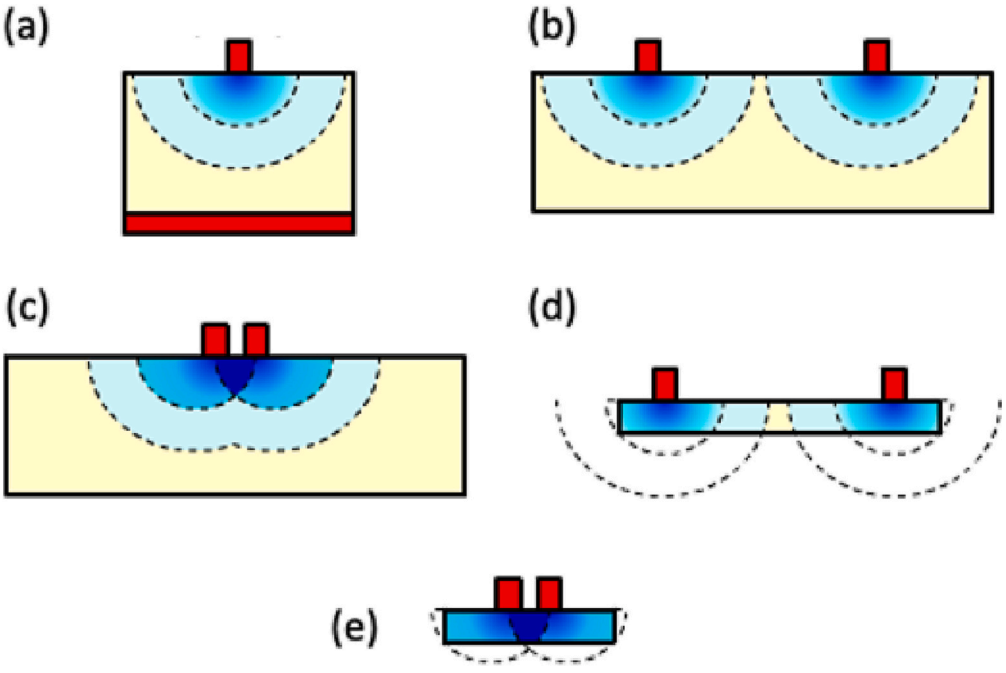

Fig. 1. Schematic illustration of two typical configurations used for micro-contact impedance spectroscopy. The spreading of the electrical current and field is depicted by circular regions emanating from the micro contact area. (a) A typical micro-top full bottom configuration and (b) a micro top-top system. (c-e) Examples of how different levels of interference and confinement can be generated. Case (c) shows how placing the contacts too close together leads to high interference but low confinement if contacts are away from external surfaces. Case (d) highlights where a large separation between the electrodes has reduced interference but generates high confinement due to the proximity of the contacts to the external surfaces. Case (e) shows how both can be present and significant in the same configuration.

As a crack in a material is a void, its volume effectively denies the flow of any current through it. This means it acts as a type of confinement like the external surfaces of the model but is between the contacts. Crack dimensions, distribution and topology within a sample will be very dependent on the specific sample under study and how it has been fabricated. Cracks may have almost the same depth as the sample thickness or be shallow, surface defects of various widths. We define a different term of *hindrance*, to describe how the size of a crack can alter the current flow around it. It is therefore important (in the first instance) to study confinement effects associated with a single crack systematically as a function of crack dimensions and S/r. This will lead to a better understanding of how possible confinement and hindrance effects caused by a crack can interact with the current interference effects from the micro-contacts for the low S/r values often employed in MCIS measurements.

Here we aim to investigate the effects generated by the presence of a crack on top-top MCIS data based on a homogenous cubic model with the electrical properties of $SrTiO_3$ at 300 °C. We use FEM to create a crack of different depths and widths in the homogenous cube, and systematically analyse the changes in impedance data for top-top MCIS measurements as a function of its dimensions and S/r. We assess the validity and applicability of the geometric factor and spreading resistance equations for extracting conductivity values under these conditions.

2. Model set up

The key aspects for the geometry of the model are shown in Fig. 2(a). Firstly a cube of side length 200 μm is created. We set this as an isotropic homogeneous material assigned with a conductivity $\sigma = 13.6$ μS/m and a relative permittivity of $\varepsilon_r = 162$. These values were experimentally determined for a $SrTiO_3$ single crystal sample at 300 °C from conventional Impedance Spectroscopy measurements [18]. Secondly, two circular electrodes are placed on the top surface of radius, r= 5 μm. We denote the shortest distance between the electrode edges as the separation, S. Finally, after the model structure has been created we discretized this structure into tetrahedron elements (a finite element mesh) using the package Gmsh [19] and simulate the electrical response of dielectric materials using an in-house developed package called Elcer [16]. This package uses Maxwell's equations to simulate the electrical responses of materials with various electrical properties and microstructures. The data generated includes electric field and current density vector maps as shown in Fig. 2(b) along with corresponding impedance spectra as shown in the results section.

A void can now be placed between the electrodes to simulate a crack, hindering the electrical flow between the two contacts. Two ways of representing this crack are as a material with the properties of air or as a void (an unmeshed region with appropriate boundary conditions) as shown in Fig. 2(c). Simulations studies of these two cases showed there was no significant difference in the converged results between the cases across a range of geometries, an example of this is shown in the Supplementary Information, SI, Fig. S1. As the void model requires fewer

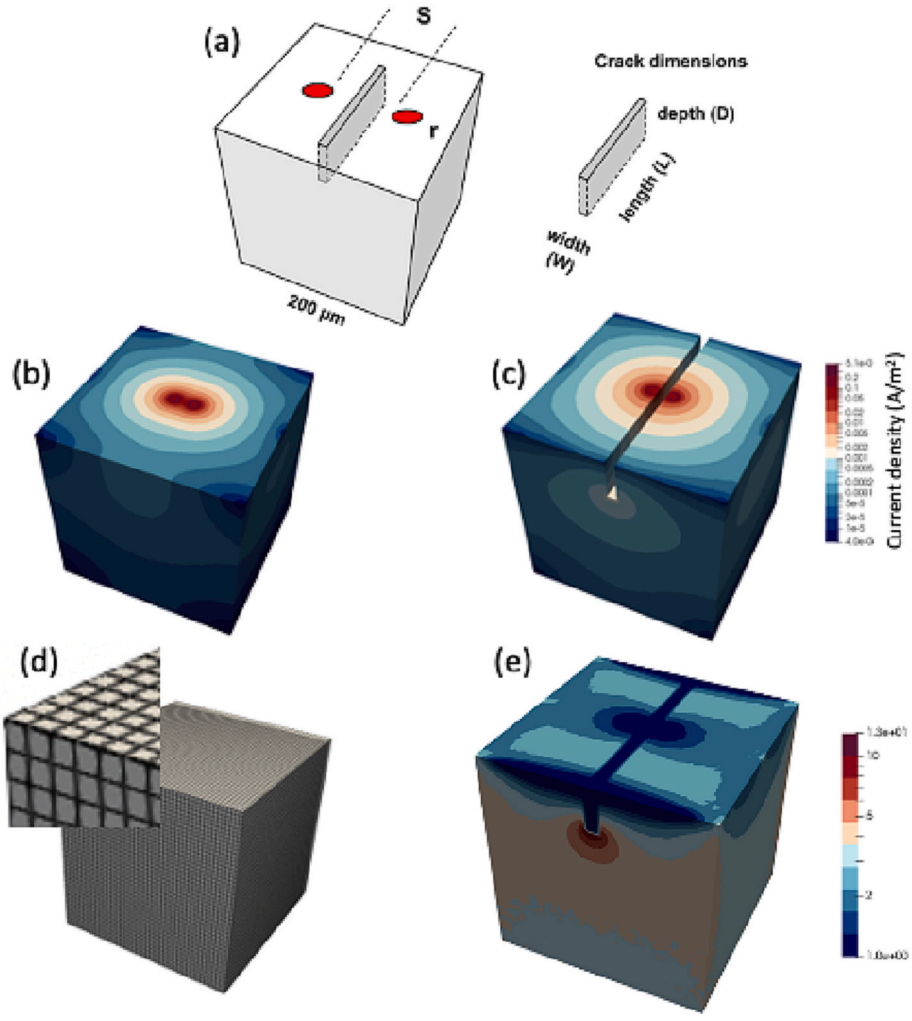

Fig. 2. (a) Schematic illustration of the model and dimensions of the crack and contacts; (b) and (c) show the current density distribution of a model with no crack and one with a crack depth of 40 μm and width of 9 μm, respectively. (d) Shows the integration points and (e) highlights the difference in current density of the crack normalised by the uncracked model (i.e. the results of figure (c) divided by figure (b)). A value of 1 represents regions of no change between the models. The crack is also set at unity.

elements, saving computational time, we present results for this representation.

Once solved using ElCer we can visualize the current density distribution maps using ParaView [20] as shown in Figs. 2(b) and (c). It is hard to directly visualize what effect the crack has on the current density. As such we use a reduced analysis by normalising the electrical response for a cracked model against its unracked equivalent. As each finite model is meshed individually, the exact location of the current density values vary as the finite element method provides a solution only on each vertex on every tetrahedron. In order to be able to divide the two solutions, the current density map for each model has to be integrated using a gaussian quadrature approach, onto a regular three-dimensional grid of points as shown in Fig. 2(d). To maintain accuracy of the results, we integrate over a 50x50x50 grid of points. This produces a solved current density map on a regular grid which allows the vector field for the model with a crack present to be normalised (divided) by its equivalent uncracked model at each grid point.

The current density in the cracked model is always higher than the uncracked counterpart with the exception in the cracked region. A value of 1 indicates where the current density in the uncracked model is equivalent to the simulation with a crack present and for simplicity the crack also appears as a value of unity. A value of 2 would for example indicate where the regions of current density are twice as high compared to the no crack counterpart. An example of this is shown in Fig. 2(e), which integrates the data from Figs. 2(b) and (c) and normalises them. This clearly shows the increased current density around the crack with little change around the contacts.

There are four key geometries changed within the modelled structures. These are the depth, width and length of the crack along with the S/r ratio of the electrodes. For clarity in identifying and following these changes we use the following definitions.

- D: the depth of the crack. This ranges from 5 to 40 μm which is equal to 1 to 8 times the electrode radius. A depth of 5 μm is denoted D5.
- W: the width of the crack. This ranges from 10 to 90% of the electrode separation. Although thinner values are more realistic for cracks, thicker voids are studied. A width of 10% is denoted W1.
- L: the length of the crack positioned centrally to the contacts. This ranges from 10 to 200 μm for the length of the model. A crack length of 200 μm which extends from one side of the model to the other is denoted by L200.
- S/r: this ratio was set as 2, 4, 6, 8, 10 and 12 to investigate how the distance to contact radius ratio influences the measured electrical properties in the presence of a crack between the electrodes.

Simulated impedance data from all models showed a single arc in complex impedance plane plots, Z*, a single plateau in spectroscopic plots of the real part of the complex capacitance, C′, and a single Debye peak in the imaginary parts of the complex impedance, Z" and electric modulus, M". All data were therefore analysed on an equivalent circuit based on a single, parallel Resistor-Capacitor, RC, element. The intercept on the real axis of the Z* plots (Z') was used to obtain R. C was calculated using the following relationship from the top of the Z* arc (i.e. Z''_{max})

$$\omega RC = 1 \tag{4}$$

where $\omega = 2\pi f_{max}$ and f_{max} is the frequency (in Hz) at Z''_{max}. The characteristic relaxation time or time constant, τ, is given by,

$$\tau = RC = \frac{1}{2\pi f_{max}} \tag{5}$$

To evaluate the influence of a crack on the impedance data from the various models, a numerical method was employed. This method compared the percentage change of the Z' intercept in the Z* plots from the models with a crack to the pristine cubic model without a crack, as shown in Eq. 6. The percentage change in the measured resistance of the models (%R) when the crack geometry was altered could therefore be quantified.

$$\%R = \frac{Z'_{Crack} - Z'_{Pristine}}{Z'_{Pristine}} \text{ x } 100 \tag{6}$$

The R values extracted from the Z* were converted into conductivity values, σ, using

$$\sigma = \frac{1}{2rR} \tag{7}$$

The conductivity of each crack model was then compared to the actual material conductivity from the pristine model (13.6 μS/m) to quantify a percentage change in conductivity compared to the pristine model as shown by the equation below.

$$\%\sigma = \sigma_{crack}/\sigma_{pristine} \text{ x } 100 \tag{8}$$

This allowed a wide range of experimental set-ups and crack conditions to be evaluated and to assess the validity and accuracy of using the spreading resistance, eq. (3), to convert R values obtained from MCIS data from eq. (4) into conductivity values, σ, eq. (7).

As each model will possess different levels of interference and confinement, we propose three new variables to help in the analysis. These are:

(i) current interference (CI);
(ii) crack effect against pristine model (CEP); and
(iii) the percentage change in calculated conductivity effect (CCE).

These variables allow us to quantify the balance between current interference and crack hindrance along with showing the combined effect on the extracted material conductivity. All conductivity values are calculated using the spreading resistance equation, eq. (7). CI compares the conductivity of the pristine model without a crack to the intrinsic conductivity assigned to the model and is defined as

$$CI = \frac{\sigma_{pristine} - \sigma_{intrinsic}}{\sigma_{intrinsic}} \times 100\% \tag{9}$$

CEP measures when a predetermined sized crack is placed into the model and how the measured conductivity changes against a pristine model without a crack, at the same S/r. CEP quantifies how much the presence of a crack can affect current flow, in other words, its hindrance ability.

$$CEP = \frac{\sigma_{crack} - \sigma_{pristine}}{\sigma_{pristine}} \times 100\% \tag{10}$$

CCE is calculated by comparing the conductivity of a model with a crack to the intrinsic conductivity assigned to the material. CCE reflects the combined effect of current interference and crack hindrance of the current.

$$CCE = \frac{\sigma_{crack} - \sigma_{intrinsic}}{\sigma_{intrinsic}} \times 100\% \tag{11}$$

3. Results and discussion

Due to the large range of possible values for the crack width, depth, and length along with changes in the S/r ratios, we limit our study in the main article to values that identify the general and significant behaviour. Large S/r ratios are often challenging to fabricate experimentally due to the physical constraints of a sample. Although higher S/r ratios (S/r = 4 to 12) have been studied, they show similar trends as that for S/r = 2, but with reduced impact due to the lower interference between the electrodes. As such we focus the results for S/r = 2 and study larger S/r using eqs. (9–11) later.

To study the effects of hindrance, confinement, and interference we set the micro top-top electrode configuration to be S/r = 2 (S = 10 μm

and $r = 5$ μm) on a cube of 200 μm. This provides a strong interference effect between the electrodes but with little confinement allowing us to probe the effect of crack hindrance on the electrical response.

We first start by looking at how the combination of width and depth of a crack can affect the electrical response. Fig. 3(a-d) presents the normalised current density plots. These show the effect of hinderance on the model due to changes in the crack width when set at W = 1 μm Fig. 3 (a,b) and W = 9 μm Fig. 3(c,d), along with crack depths set at D = 5 μm Fig. 3(a,c) and D = 40 μm Fig. 3(b,d). All plots are normalised to the pristine sample, which is a simulation of the electrode configuration (S/r = 2) in the absence of a crack. The associated impedance responses are shown in Fig. 3(e-f) for Z* plots and C′ spectra, respectively. Within the SI, Fig. 3(a) and (c) can be seen scaled to their maximum value for clarity, Fig. S2 along with further data plotted in other formalisms, Fig. S3. In all cases a single and ideal arc is obtained in Z* plots shown in Fig. 3(e) along with a single plateau in C′ spectra, Fig. 3 (f). Resistance and capacitance values are extracted through the intercept of the real axis on Z* and the plateau in C′, respectively.

We start with a thin shallow crack, D5W1, as shown in Fig. 3(a). There is very little change in the current density due to the presence of the crack. An increase in normalised current density is measured to reach a maximum of 1.2×, found directly below the crack. This is due to its hindrance which causes the external bottom surface to experience a small increase of 1.1× that of the pristine sample. This small change in current density highlights there is little change in the confinement and interference of the model and is in good agreement with the confinement study reported by Veazey et al. [18]. The impedance response also experiences a change with the associated resistance. The resistance of the pristine model was 5.0 GΩ and increased to 5.4 GΩ with the presence of the thin shallow crack. The associated capacitance decreases as shown by the decrease in plateau height in C′ spectra Fig. 3(f) from 2.1×10^{-14} to 1.9×10^{-14} F. It is important to note that τ, the product of RC remains constant. This is reflected in the f_{max} value of 1526 Hz in the Z* plots which is invariant across all models and is in good agreement with the theoretical value of 1500 Hz. This change in R and C reflects a change in volume fraction of the homogeneous material in the model and plays a dominant role under the conditions employed in these models. A similar result is observed for a wider shallow crack, D5W9. Here the hindrance increases the normalised current density under the crack to a factor of 1.5× (1.2× at the lower surface) compared to that of the pristine sample, but we begin to observe the effect that the crack has on the confinement, with the increased current density extending down the length of the crack towards the external surfaces. This combination of hindrance and enhanced confinement increases R to 6.4 GΩ but again maintains the ideal, Debye-like single response with the f_{max} value of 1526 Hz unchanged due the corresponding decrease in capacitance.

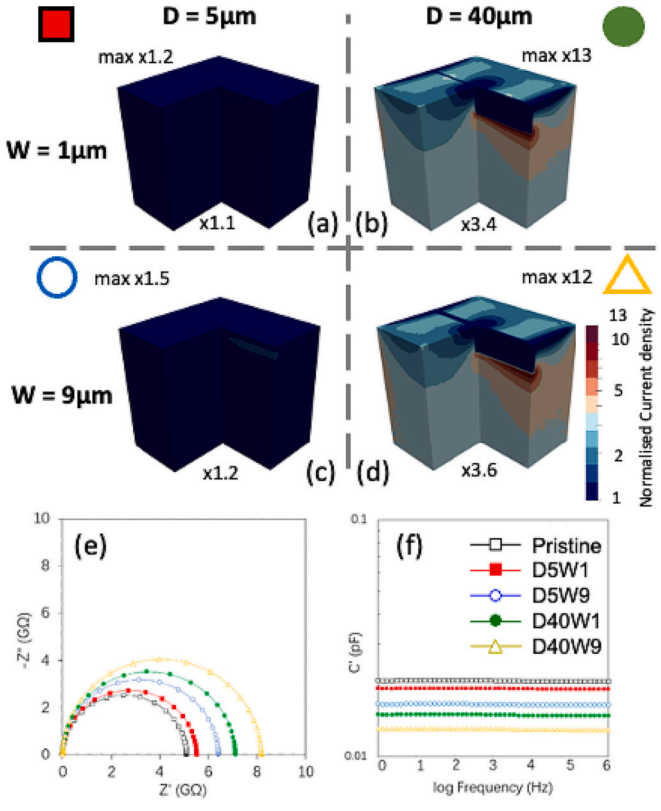

Fig. 3. (a) The effect of crack width and depth on the current density and impedance data. (a)-(d) highlight the normalised current density. Annotated is the maximum normalised factor within the model along with the value measured at the lowest surface to provide an indication of the confinement current. Parts (e) and (f) show the corresponding impedance data.

Changes in the crack depth play a more significant role. We increase the depth of the crack from 5 to 40 μm, which is 8× the radius of the contacts. In Fig. 3(b) a thin deep crack D40W1, clearly shows significant changes in the current density due to the presence of the crack's hindrance. Firstly, the hindrance generates a maximum normalised current density increase of 13× that is generated directly under the crack between the electrodes but extends out towards the external lower surface, reaching a value of 3.4×. This surge in current density is consistent with the current having to detour around the crack to reach the opposing electrode. This rise in current density at the external surfaces also provides an enhancement to the confinement of the sample and increases the resistance to 7.1 GΩ. It is worth noting that no significant change(s) is measured around the contacts, highlighting little change in the interference effect caused by the electrode configuration of S/r = 2. A similar significant change is also seen in a wide deeper crack of D40W9 as shown in Fig. 3(d). Although the current density maximum directly under the crack falls to 12× compared to the narrow crack (13×), there is a greater current density enhancement on the external surfaces, where the lower surface experiences a larger change of 3.6×. This gives rise to further enhancement of confinement and as such a larger rise in resistance. A comparative figure for S/r = 12 can be found in SI, Fig. S5.

In extracting the electrical properties from the impedance responses, the spreading resistance eq. (3) has been widely used to calculate conductivity when top-top micro-contacts are used for nominally pristine samples without defects. The underlying assumptions in the derivation of the equation are that the electrical properties of the sample are homogeneous with no resistive layers or electrical heterogeneity existing between the two electrodes. To the best of our knowledge, there exists no reports on applying the spreading resistance equation on micro-contact measurements with cracks.

As seen in the impedance, both the crack depth and width increase the Z' intercept and overall measured resistance. Here we now quantify the relative increase in resistance (%R) and its associated effect on %C and extracted conductivity (%σ). The results in Fig. 4 are presented against %(crack width/electrode separation) and are grouped by different depths to radius ratios. For example, a depth/radius = 1 has a crack depth of 5 μm whereas D/r = 8 has a crack depth of 40 μm.

The smallest rise in R (~8%) occurs in the minimum crack dimensions of width = 10% separation and depth at 1× of the electrode radius. The maximum change of %R (~60%) occurs in the largest crack dimensions with width 90% of the electrode separation and depth at 8× of the electrode radius. As f_{max} remains constant throughout, the time constant of all models is insensitive to the inclusion of a crack. This is shown in Fig. 4(b) where all data points are superimposed such that only the pristine data are visible. Thus, due to the relationship in eq. 5, if %R increases, an associated decrease occurs in %C, Fig. 4(c). As the crack depth increases from 5 to 20 μm the relative increase in R is significant but beyond 20 μm (4 times the contact radius), the rate of increase is slower. This illustrates the hindrance effect of the crack depth. Furthermore, after a crack depth of 20 μm, the hindrance causes the

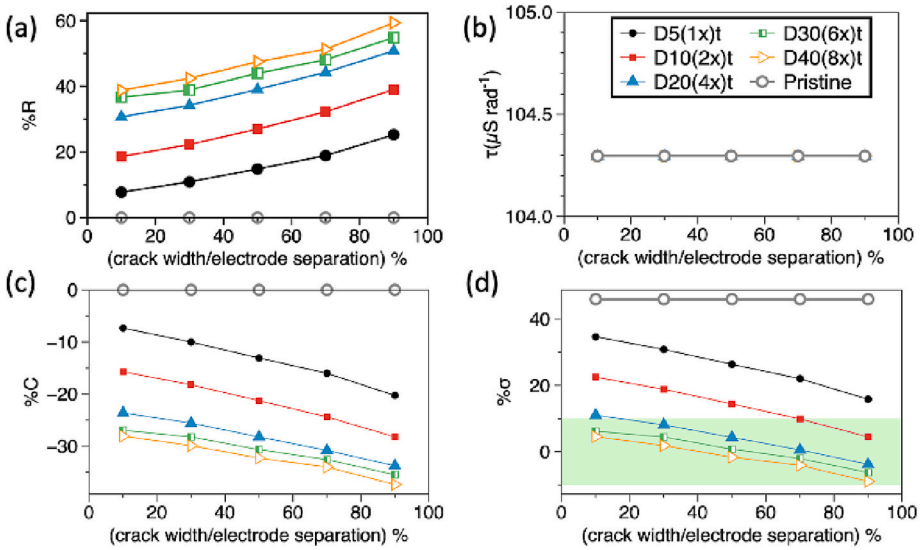

Fig. 4. The change in electrical properties as a function of %(crack width/electrode separation). (a) The change in R as %R to show the crack width effect in the strong interference model. (b) The time constant, τ and (c) the extracted change in C shown as % C. (d) The extracted %σ using the spreading resistance equation and compared to the conductivity assigned to the model where the green shaded area indicates where the spreading resistance equation gives results within ±10% of the input value. The hollow circles represent results from a pristine model. All other lines are shown to guide the eye. (For interpretation of the references to colour in this figure legend, the reader is referred to the web version of this article.)

current density to increase in regions away from the crack restoring some portion of current flow.

The associated %σ extracted from R using eq. (7) is shown in Fig. 4 (d). Please note the grey data set, which shows the enhanced conductivity associated with the interference from a pristine model. With increasing crack depth and width, the hindrance of the crack on the current flow begins to offset the electrode interference. When the crack width is at 80% (W8) of electrode separation and a depth 4 times the electrode radius, (D20) the difference between the calculated and actual conductivity value is negligible. For larger crack dimensions, %σ becomes negative indicating the hindrance effect exceeds the interference associated with S/r = 2. If we consider conductivity values within 10% of the actual value are acceptable, then the spreading resistance equation is seen to be accurate in a few cases. When the crack depth to electrode radius ratio is 4 and above, almost every model with any crack width could give a relatively accurate conductivity result. Accurate results for D5 models containing a crack with D/r = 1 could not be obtained for any width; however, when the crack depth is doubled, D10 models with a crack width of ≥70% can provide accurate results.

To quantify the levels of confinement and interference of a crack, a series of models with increasing S/r were generated. The crack depth was fixed at 20 μm along with a width of 1 μm, which is 10% of the electrode separation. As S/r increases, the width of the crack increases proportionally but the crack depth is fixed. Eqs. (9–11) were applied to calculate CI, CEP and CCE. CI decreases as S/r increases from ~45% (S/r = 2) to ~23% (S/r = 12) and the crack effect also diminishes CEP from ~24% (S/r = 2) to only ~3% (S/r = 12), Fig. 5 (a). Although CI and CEP both decrease by ~22%, the crack effect is becoming less effective in balancing the current interference. This is reflected in the increase of CCE as S/r increased, Fig. 5 (a). It is noteworthy that beyond S/r = 6, CCE remains relatively constant near ~20%, suggesting a balance between CEP and CI is obtained.

In the scenario of a wider crack, the crack width was increased from 10 to 90% of the total separation. For S/r = 2, the crack width is 9 μm and for S/r = 10 it is 45 μm, Fig. 5 (b). The crack depth is again fixed at 20 μm to reduce the number of variables. In this case, the hindrance of the proportionally wider crack is strong enough to compensate the current interference from the electrodes when S/r increases with calculated conductivities being within 5% error of the intrinsic material value. However, it is an unlikely scenario to find such a large width crack and to perform MCIS measurements around it. Overall, this current interference versus crack effect study shows that as the separation between the micro-contacts increases, the current interference decreases. This agrees with existing literature [18]. The confinement effect

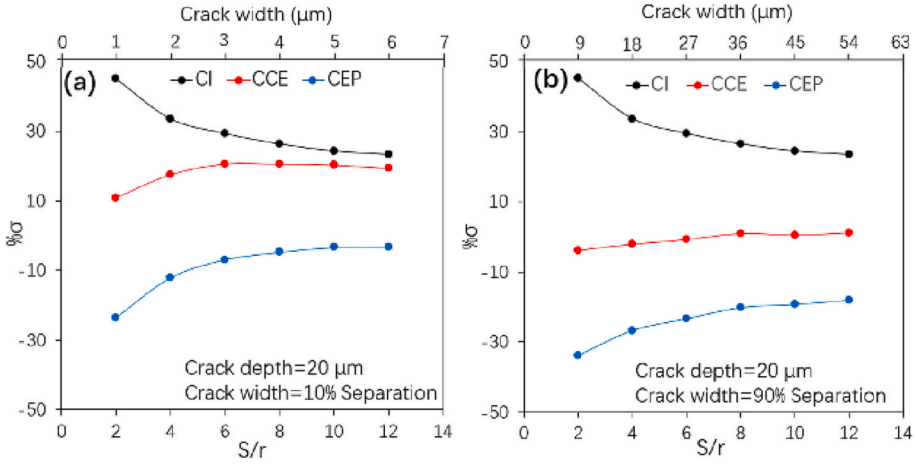

Fig. 5. Current Interference (CI), crack effect against pristine model (CEP) and calculated conductivity with the crack effect (CCE) plotted versus S/r. (a) The crack depth of all models is fixed at 20 μm and the crack width is fixed at 10% of the electrode separation. (b) All models contain a crack with a width of 90% of electrode separation rather than 10% for the models in (a).

of the crack over current flow also decreases with increasing S/r. The balance between current interference and crack confinement can be a delicate balance when certain crack (or any resistive region) size requirements are met, e.g., at 90% of electrode separation.

So far, we have shown that the crack depth generates a greater hindrance than the width of the crack. We now study the influence of the hindrance due to the length of the crack.

We set the width to 1 μm (W1) and the depth to 20 μm which corresponds to 4r (D20). Fig. 6(a-d) shows how the crack length effects the normalised current density, and Fig. 6(e-f) the associated impedance spectra for S/r = 2. Fig. 6(a-b) are shown in SI in Fig. S6 scaled to their individual maximum for additional clarity. As before, a single arc in the impedance is generated with the time constant remaining independent of the study. For cracks below a length of 20 μm, there is little change in the measured normalised current density, with a corresponding small change in the impedance spectra. At a length of 20 μm, the hindrance causes the maximum normalised current factor to rise to 2.3× and is primarily around the side and bottom of the crack, Fig. 6(a) inset, with an increase of 1.2× in the current density at the external bottom surface, indicating greater confinement current. Little change is observed in and around the area of the contacts which highlights that the hindrance effect is much smaller compared to the high contact interference. This hindrance does, however, lead to an increase in the confinement, increasing R from 5.0 GΩ (pristine) to 6.0 GΩ. As the cracks length increases, the hindrance also increases causing the normalised current density factor to continue to increase. At a crack length of 100 μm, the maximum normalised current density increases to 9× of the pristine model. There is also a greater confinement current as the bottom external surface experiences a rise in current density by 1.8× compared to the pristine model and increases the resistance to 6.6 GΩ. At 200 μm, we note the maximum normalised current density drops to a factor of 6. This is due to the crack extending to the edge of the model and the current not being able to flow around it. However, as the current can now flow only under the crack, the hindrance still increases the confinement compared to a pristine sample, albeit at a slower rate. For completeness, the effect of crack length on the current density and impedance data for D20W1 models for S/r = 12 are provided in SI, Fig. S7.

We highlight the changes in R and C along with the extracted conductivity, σ, in Fig. 7. The trend is very similar to the effects of crack depth with an increase in %R and an associated decrease in %C, as

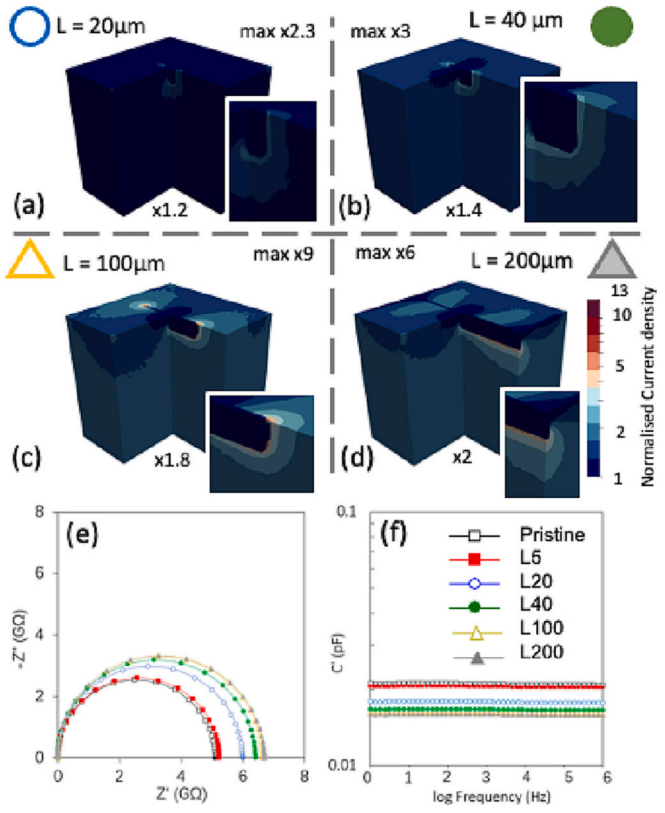

Fig. 6. (a) The effect of crack length on the current density and impedance data for D20W1 models for S/r = 2. (a)-(d) Normalised current density for the various models. (Inset) A zoom view of the crack. Each part is annotated with the maximum normalised factor within the model along with the value measured at the lower external surface. Parts (e) and (f) show the corresponding impedance data for the various models.

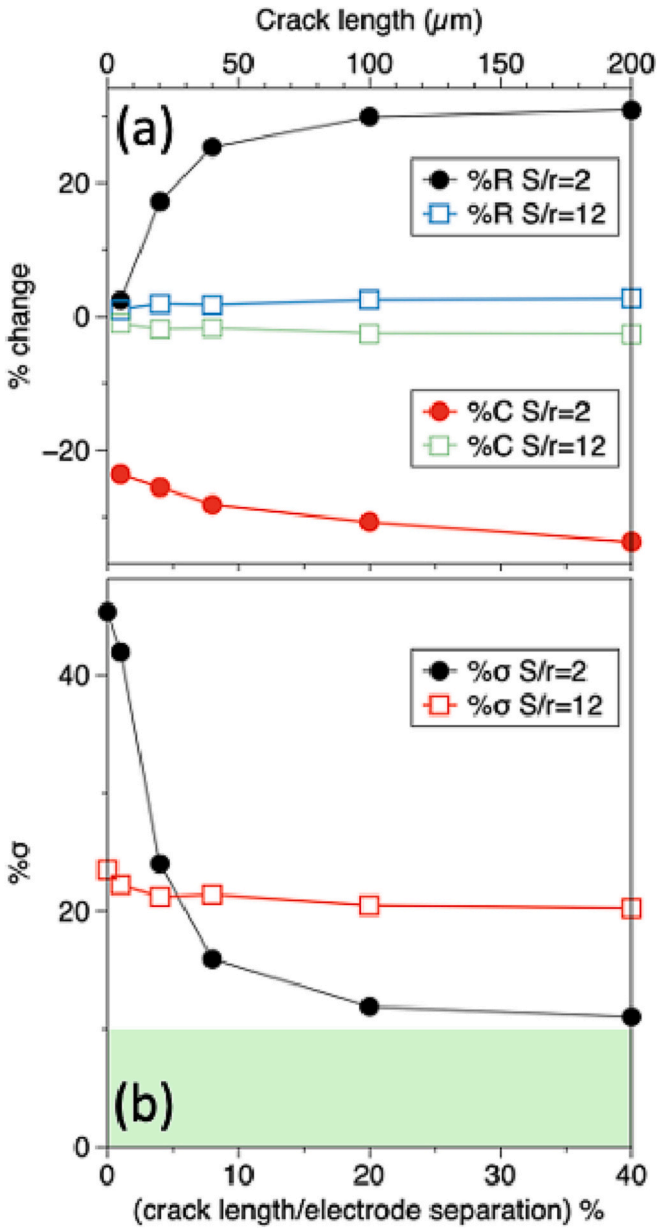

Fig. 7. The change in electrical properties as a function crack length / electrode radius. (a) The %change of R and C with respect to the pristine model for two different S/r ratios, and (b) the extracted %σ using the spreading resistance and compared to the conductivity assigned to the model. The green shaded area indicates where the spreading resistance equation gives results within ±10% of the input value. The lines are added as guides for the eye. (For interpretation of the references to colour in this figure legend, the reader is referred to the web version of this article.)

shown in Fig. 7(a). When the crack length is the same size as the contact (5 μm), there is less than a 1% change in %R. As the crack increase to 4 times the radius (20 μm) the hindrance causes %R to increase rapidly to ~17%. This increase continues and slowly plateaus to the full crack model at 200 μm, where %R is over 30% compared to the pristine sample. In Fig. 7(b), the conductivity is extracted using the spreading resistance equation. As the length increases to 20 times the radius, the initial overestimate of the conductivity is reduced to be close to 10%. We also include in Fig. 7, how the S/r ratio influences this effect. At S/r = 12 the enhancement due to the crack's hindrance is much reduced with little change in the current density and a reduced change in both %R and %C by <5%. The hindrance and confinement generated is now no longer at a level to counteract the interference, and the error in conductivity remains at ~20%.

We now apply CI, CEP and CCE respectively to establish how the crack length affects the confinement and interference. These are shown in Fig. 8 for two different S/r ratios. As the interference between the contacts is independent of crack length, CI results in fixed ~45 and ~ 23% over estimation of conductivity for S/r = 2 and 12, respectively. For an S/r ratio of 2, increasing the crack length reduces CCE from ~42 to ~10% as the crack extends to 20× that of the contact radius due to the strong CEP response, Fig. 8. This shows how a change in crack length could offset the interference between the contacts and lead to a near acceptable conductivity value. For S/r = 12, the crack is less influential as shown by small changes in CEP and therefore CCE shows very little reduction with increasing crack length, Fig. 8. CCE therefore remains relatively constant with a ~ 20% discrepancy to the correct conductivity value. This current interference versus crack length study follows the same trend as that shown for crack depth: as the micro-contact separation increases, the current interference decreases.

Overall, the crack geometries investigated here have a width of 1 μm or greater. To observe how nano-sized cracks influence impedance data

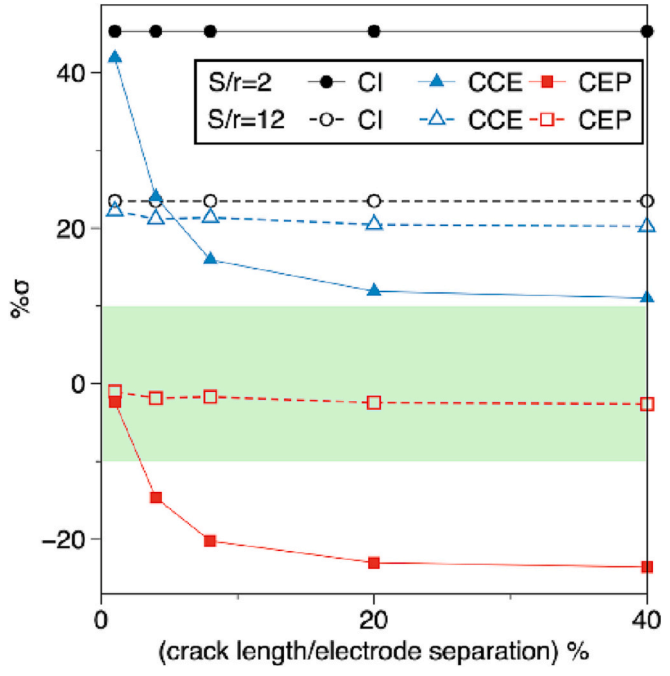

Fig. 8. Current Interference (CI), crack effect against pristine model (CEP) and calculated conductivity with the crack effect (CCE) plotted versus crack length / electrode radius values for S/r = 2 (filled shapes, solid lines) and S/r = 12 (unfilled shapes, dashed lines). The green shaded area indicates where the spreading resistance equation gives results within ±10% of the input value. The lines are added as guides for the eye. (For interpretation of the references to colour in this figure legend, the reader is referred to the web version of this article.)

an S/r = 2 model was created for a crack that spans the entire length of the sample and is 20 μm deep. Using structured prism elements, the crack width was meshed from 200 nm down to 10 nm. Properties of air were assigned to this region as $\sigma = 0.5 \times 10^{-14}$ S/m and $\varepsilon_r = 1$, consistent with previous simulations of porosity [21]. To ensure convergence and reliability in the results, we generate at least 5 layers of elements through the width of the crack.

The results obtained are shown in Fig. 9 along with a simulation for the pristine model which is used for comparison. The pristine model produces an ideal Debye-like response with intercepts giving $R = 5.8$ GΩ and $C = 1.8 \times 10^{-14}$ F. When a 200 nm crack is introduced between the contacts, a small non-ideal distortion in the Z* plot is generated, however this gives rise to a 14% decrease in bulk capacitance to $C = 1.68 \times 10^{-14}$ F, Fig. 9(b), along with a 20% increase in resistance of the sample to $R = 7.3$ GΩ, Fig. 9 (a). As the crack decreases in width, the resistance of the system remains unchanged whereas the value of the high frequency plateau in C′ begins to increase towards that of the (pristine) bulk. As this occurs however, a clear, low frequency and high capacitance plateau is formed, Fig. 9 (b). This response can be attributed to the presence of the crack and a capacitive short circuiting due to the permittivity of the air. At crack widths below 20 nm, a clear second response is now directly observed in the Z* plots, Fig. 9 (a). As the distortion now moves away from the bulk response, the extracted values of R and C are within 2% of the pristine sample. Further detailed investigation into this effect are in progress.

4. Conclusions

A finite element model has been developed to investigate the influence of a surface crack (void) in a homogeneous material on top-top microcontact impedance spectroscopy measurements. The crack was placed between the micro-contacts and the variables studied were the S/r of the micro-contacts and the crack dimensions (i.e. depth, width and length). The results were compared against a pristine model (no crack) with the same electrode arrangements. This allowed hindrance effects associated with a crack of variable dimensions to be considered in the presence of current interference and confinement effects associated with variable S/r values in top-top MCIS measurements.

In general, the strong interference effects associated with low S/r that give rise to enhanced conductivity values in pristine models can be counterbalanced by the hindrance of the crack. Although the crack width does alter the impedance response, it is not as influential as the crack length and depth, which provide significant changes. Both current interference and crack hindrance decrease with increasing S/r. This demonstrates that when interrogating the electrical properties of materials with local contacts, if cracks are present within the specimen, they may fortuitously assist in offsetting significant current interference effects, especially at the low S/r values (≤6) used in many experimental set-ups.

CRediT authorship contribution statement

Hong Ma: Conceptualization, Methodology, Software, Investigation, Data curation, Visualization, Writing – original draft. **Derek C. Sinclair:** Conceptualization, Methodology, Supervision, Writing – review & editing, Project administration, Funding acquisition. **Julian S. Dean:** Conceptualization, Methodology, Software, Supervision, Formal analysis, Writing – review & editing, Visualization.

Declaration of Competing Interest

The authors declare that they have no known competing financial interests or personal relationships that could have appeared to influence the work reported in this paper.

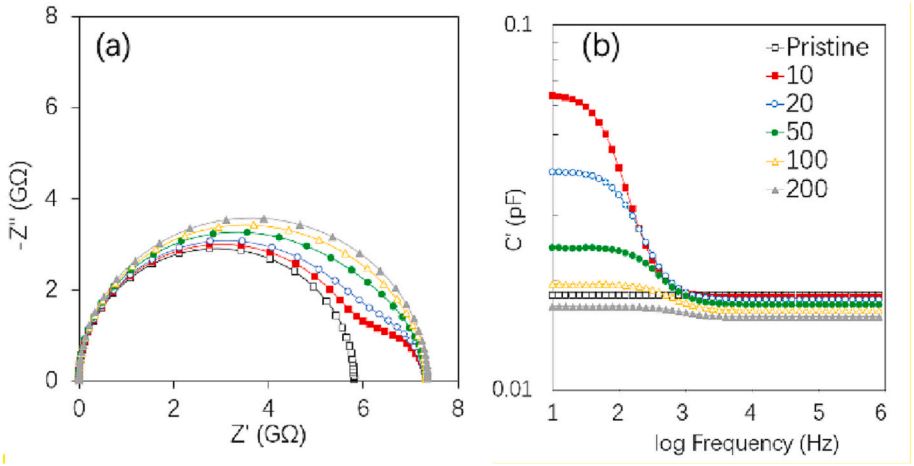

Fig. 9. Simulated impedance response in (a) Z* and (b) C′ spectra from the presence of nano-cracks highlighting how capacitive short circuits can occur for very thin (nano) cracks.

Data availability

Data will be made available on request.

Acknowledgements

The authors wish to thank the referees for very useful comments on the script and especially their comments and suggestions on the influence of nano-cracks on the impedance response.

Appendix A. Supplementary data

Supplementary data to this article can be found online at https://doi.org/10.1016/j.ssi.2023.116173.

References

[1] J.T.S. Irvine, D.C. Sinclair, A.R. West, Electroceramics: characterization by impedance spectroscopy, Adv. Mater. 2 (1990) 132–138.
[2] D.C. Sinclair, A.R. West, Impedance and modulus spectroscopy of semiconducting barium titanate showing positive temperature coefficient of resistance, J. Appl. Phys. 66 (1989) 3850–3856.
[3] S.I. Costa, M. Li, J.R. Frade, D.C. Sinclair, Modulus spectroscopy of $CaCu_3Ti_4O_{12}$ ceramics: clues to the internal barrier layer capacitance mechanism, RSC Adv. 3 (2013) 7030–7036.
[4] R. Holm, Electric Contacts, Springer, 1967.
[5] J. Fleig, J. Maier, Local conductivitiy measurements on AgCl surfaces using microelectrodes, Solid State Ionics 85 (1996) 9–15.
[6] J. Fleig, J. Maier, Microcontact impedance measurements of individual highly conductive grain boundaries: general aspects and application to AgCl, Phys. Chem. Chem. Phys. 1 (1999) 3315–3320.
[7] J. Fleig, Microelectrodes in solid state ionics, Solid State Ionics 161 (2003) 279–289.
[8] J. Fleig, In *Advances in Electrochemical Science and Engineering*, Wiley-VCH, 2002, pp. 1–79.
[9] E. Navickas, M. Gerstl, G. Friedbacher, F. Kubel, J. Fleig, Measurement of the across-plane conductivity of YSZ thin films on silicon, Solid State Ionics 211 (2012) 58–64.
[10] S. Taibl, G. Fafilek, J. Fleig, Impedance spectra of Fe-doped $SrTiO_3$ thin films upon bias voltage: inductive loops as a trace of ion motion, Nanoscale 8 (2016) 13954–13966.
[11] M. Shirpour, R. Merkle, C. Lina, J. Maier, Nonlinear electrical grain boundary properties in proton conducting Y–$BaZrO_3$ supporting the space charge depletion model, Phys. Chem. Chem. Phys. 14 (2012) 730–740.
[12] H. Bishara, H. Tsybenko, S. Nandy, Q.K. Muhammad, T. Frömling, X. Fang, J. P. Best, G. Dehm, Dislocation-enhanced electrical conductivity in rutile TiO_2 accessed by room-temperature nanoindentation, Scr. Mater. 212 (2022), 114543.
[13] J.-S. Lee, J. Fleig, J. Maier, D.-Y. Kim, T.-J. Chung, Local conductivity of nitrogen-graded zirconia, J. Am. Ceram. Soc. 88 (2005) 3067–3074.
[14] N. Wu, K. Ogawa, M. Chyu, S.X. Mao, Failure detection of thermal barrier coatings using impedance spectroscopy, Thin Solid Films 457 (2) (2004) 301–306.
[15] J. Maier, J. Fleig, Point contacts in solid state ionics: finite element calculations and local conductivity measurements, Solid State Ionics 86–88 (1996) 1351–1356.
[16] J.S. Dean, J.H. Harding, D.C. Sinclair, Simulation of impedance spectra for a full three-dimensional ceramic microstructure using a finite element model, J. Am. Ceram. Soc. 97 (2013) 885–891.
[17] P. Heath, J.S. Dean, J.H. Harding, D.C. Sinclair, Simulation of impedance spectra for core-shell grain structures using finite element modeling, J. Am. Ceram. Soc. 98 (2015) 1925–1931.
[18] R.A. Veazey, A.S. Gandy, D.C. Sinclair, J.S. Dean, Modeling the influence of two terminal electrode contact geometry and sample dimensions in electro-materials, J. Am. Ceram. Soc. 102 (2019) 3609–3622.
[19] C. Geuzaine, J.-F. Remacle, Gmsh: a three-dimensional finite element mesh generator with built-in pre- and post-processing facilities, Int. J. Numer. Methods Eng. 79 (11) (2009) 1309–1331.
[20] Kitware Inc, Paraview [Online]. Available, https://www.paraview.org/ [Accessed 20 1 2022].
[21] G. Dale, M. Strawhorne, D. Sinclair, J. Dean, Finite element modeling on the effect of intra-granular porosity on the dielectric properties of $BaTiO_3$ MLCCs, J. Am. Ceram. Soc. 101 (2018) 1211–1220.